Mon. Not. R. Astron. Soc. **000**, 000–000 (0000) Printed 19 February 2014 (MN LATEX style file v2.2)

Mass-Galaxy offsets in Abell 3827, 2218 and 1689: intrinsic properties or line-of-sight substructures?

Irshad Mohammed⋆,[1] Jori Liesenborgs,[2] Prasenjit Saha[1] and Liliya L. R. Williams[3]
[1] *Institute for Theoretical Physics, University of Zürich, 8057 Zürich Switzerland*
[2] *Expertisecentrum voor Digitale Media, Universiteit Hasselt, Wetenschapspark 2, B-3590, Diepenbeek, Belgium*
[3] *School of Physics & Astronomy, University of Minnesota, 116 Church Street SE, Minneapolis, MN 55455, USA*

19 February 2014

arXiv:1402.4217v1 [astro-ph.CO] 18 Feb 2014

ABSTRACT

We have made mass maps of three strong-lensing clusters, Abell 3827, Abell 2218 and Abell 1689, in order to test for mass-light offsets. The technique used is GRALE, which enables lens reconstruction with minimal assumptions, and specifically with no information about the cluster light being given. In the first two of these clusters, we find local mass peaks in the central regions that are displaced from the nearby galaxies by a few to several kpc. These offsets *could* be due to line of sight structure unrelated to the clusters, but that is very unlikely, given the typical levels of chance line-of-sight coincidences in ΛCDM simulations — for Abell 3827 and Abell 2218 the offsets appear to be intrinsic. In the case of Abell 1689, we see no significant offsets in the central region, but we do detect a possible line of sight structure: it appears only when sources at $z \gtrsim 3$ are used for reconstructing the mass. We discuss possible origins of the mass-galaxy offsets in Abell 3827 and Abell 2218: these include pure gravitational effects like dynamical friction, but also non-standard mechanisms like self-interacting dark-matter.

Key words: gravitational lensing: strong, galaxies: clusters: individual: Abell 1689, Abell 2218, Abell 3827

1 INTRODUCTION

Our current understanding of the universe and its dynamics indicates that its major components are dark: cold dark-matter (CDM) and the so-called "dark-energy". Unlike baryons, dark-matter interacts only gravitationally and provides the deep potential wells which are followed by the baryons. The baryons form clumps at these potential wells and cool down to form stars. The standard ΛCDM model explains a range of observed processes pretty well, from the angular power spectrum of the cosmic microwave background (Planck collaboration et al. 2013) to the baryonic acoustic oscillations (Sánchez et al. 2013) in the large scale structure and the number counts of clusters. However, the intrinsic properties and behaviour of dark-matter and dark-energy remain an open problem in cosmology.

In the picture of hierarchical structure formation in ΛCDM model, galaxy-clusters are the most recently formed structures that are gravitationally bound. They are cosmic laboratories to test the laws of gravity, structure formations and the interaction of different species of particles. A galaxy cluster contains lots of galaxies — tens to thousands, hot intra-cluster plasma visible in X-rays, a variety of of relativistic particles and finally dark-matter which dominates its mass budget. Measuring the mass of the galaxy-cluster is an essential aspect of using the cluster to study many other things. There are several physical processes that enable one to measure the mass: the kinematics of cluster galaxies (Saro et al. 2013), the hydrodynamics of hot gas emitting X-rays (Vikhlinin et al. 2009), and gravitational lensing. Lensing is particular interesting, because it relies only on gravity and does not itself require any luminous objects in the cluster being studied. One of the questions that lensing can address is how well the luminous matter traces the distribution of total mass. Deviations, or lack thereof, from the mass-follows-light hypothesis will provide important information about the physical processes going in within clusters. The first lensing-based detection of deviations from mass-follows-light goes back to the late 1990's (Abdelsalam et al. 1998) but the observation that generated a wide interest in these deviations was that of the

⋆ irshad@physik.uzh.ch

Bullet Cluster (Clowe et al. 2006), which showed unambiguously that dark matter is quite collisionless compared to the gas phase baryonic matter (Randall et al. 2008). While the properties of dark matter are probably not the only reason for deviations from mass-follows-light in galaxy clusters, dark matter self-interaction cross-section and how to optimally extract it from observations is an exciting avenue of research (Harvey et al. 2013b,a).

This work uses strong gravitational lensing to look for deviations from mass-follows-light, i.e. it explores the correspondence on the sky between the dark-matter peaks with the galaxies in the central parts of three galaxy clusters, Abell 3827, 2218 and 1689. These clusters are very different from each other in morphology and redshift. As we discuss in Section 4, some deviations we find may be due to the non-standard properties of dark matter, but others could be the result of superimposed substructure, or hydrodynamics within the cluster.

We use GRALE (Liesenborgs et al. 2006, 2007), a strong-gravitational lensing tool to reconstruct the mass map of the clusters. There is no overall parametric form for the mass distribution, but rather an adaptive grid. Other than the redshift, no information about the cluster is required as input, not even its location or morphology. This makes GRALE well-suited to reconstruction of mass maps before comparison with light.

2 THE LENS-RECONSTRUCTION TECHNIQUE

GRALE has been applied to other strong-lensing clusters (Liesenborgs et al. 2008, 2009) and compared with other techniques (Zitrin et al. 2010, 2011), so here we just give a general description and then some tests.

2.1 Grale

The data given to GRALE consist of the identified multiple-image systems and their redshifts, along with possible regions where additional images are guessed to be likely. No information about the light from the lens is given. The mass maps in GRALE are free-form, being made up of a superposition of many components. In the present work, each component is taken as a Plummer lens, that is, the usual Plummer sphere

$$\rho = \frac{3M}{4\pi}\frac{a^2}{(r^2+a^2)^{5/2}} \tag{1}$$

projected to two dimensions. Other choices of lens component, such as square tiles, are also possible.

Any mass distribution in GRALE is assigned a fitness with respect to the given data. The fitness has two components, as follows.

(i) For a given mass map, the input images are ray-traced back to the source, using the lens equation. The more nearly these back-projected images coincide for any multiple-image system, the fitter the mass map. If the fitness measure were simply the source-plane distance between the back-projected images, that would favour extreme magnification (tiny sources); accordingly, the fitnes measure is scaled to the source size.

(ii) There could be further places in the image plane that, when ray-traced back to the source, coincide with the sources corresponding to the observed images. These correspond to extra images, and would be favoured by the above fitness measure. There may indeed be undiscovered extra images in certain regions, but in most of the image plane, extra images can be ruled out with high confidence. The area of no images present is referred to in GRALE as the null space. For each image system, the user specifies a null space, which is simply the image plane with the images themselves cut out, and (optionally) further cutouts where incipient images could potentially be present. Images in the null space lead to a fitness penalty for the mass map.

It is possible to have other components to the fitness, such as time delays for quasar source (Liesenborgs et al. 2009), but the present work uses these two. The null space, item (ii) above, is a unique aspect of GRALE. There are other techniques that allow the mass distribution to be very general in form, as with GRALE, but they make additional assumptions in order to suppress extra images, such as constraining local density gradients (Saha et al. 2006) or applying smooth interpolation schemes Coe et al. (2008). Only GRALE incorporates the absence of images as useful data.

The computational part of GRALE is optimizing the fitness function for the given data, using a genetic algorithm. The basic idea, inspired by Darwinian evolution, is to generate a population of trial solutions. A fitness measure is assigned to each trial solution and then these solutions are combined, cloned and mutated to get the next generation of populations supported by a better fitness function. Genetic algorithms have long been used in astrophysics for hard optimization problems (for a somewhat old but readable review, see Charbonneau 1995). They tend to be computationally expensive, but are often effective on otherwise intractable problems. GRALE uses a multi-objective genetic algorithm, meaning that the different components of the fitness function are compared individually, not just combined into a single function. Only the fitness ranking matters in genetic algorithms, not the actual values of the fitness. In terms of likelihoods and posterior probabilities, models with better fitness are considered more probable, that is, the fitness components are monotonic in the posterior probability, but there is no known or assumed functional relation between likelihood and fitness.

The locations and masses of the Plummer components are chosen by the genetic algorithm. The algorithm also adapts the number of Plummers, but an allowed range is specified by the user. That is, the user specifies the level of substructure. For the GRALE fitness measure, lower is better, and it decreases as we increase the resolution of the map. This is quite intuitive as more Plummer spheres nat-

urally result in a better fit. So the overall criterion should be somehow a function of the GRALE fitness measure and the number of Plummers. We are not aware of any theoretical argument that yields the appropriate criterion, but after some experimentation we found one that works reasonably well in test cases. This is an 'unfitness' or

$$\text{badness} = \ln\left(\text{GRALE fitness} \times \sqrt{\text{number of components}}\right). \quad (2)$$

If we think of the GRALE fitness measure as a mismatch distance, and the number of Plummers as the inverse resolution length, the badness criterion appears natural.

To choose the number of Plummer components, we adopted the following procedure. First, we have GRALE reconstruct the lens with a comparatively low number of Plummers. Then we let GRALE improve the fit with progressively more Plummers, allowing more substructure to be introduced. After that, we let GRALE continue to adapt the fit with progressively fewer Plummers. The mass distribution with the minimum badness (2) is taken as the result.

We now report on two simulated lenses, which we generated and then reconstructed with GRALE, in order to check the pipeline and calibrate the error estimates.

2.2 A simple lens

A Plummer lens of mass $10^{14}\mathrm{M}_\odot$ was generated at redshift 0.1. Six sources were put at different redshifts (one at 0.15, two at 0.2, two at 0.4 and one at 1.0). The mass profile and image plane are shown in Figure 1. The images and source redshifts were given to the inversion module of GRALE. Figure 2 shows the reconstructed masses at different resolutions and the badness values.

When reconstructing the lens, GRALE did not have the information that in fact it had a simple parametric form, without substructures. The reconstructions do have some substructure, as well as small offsets from the centre. Such spurious features increase with resolution. The least-badness criterion, however, favours a model with relatively little substructure.

2.3 A more complex lens

We now increase the complexity, both of the input lens and of the reconstruction procedure. For each data set, from now on we will present a mean map Σ and a fraction rms-deviation map $\delta\Sigma/\Sigma$, obtained as follows. From the images, we first let GRALE construct a sequence of maps at nine different resolutions (as with the simple lens), and then select the one at minimum badness. This whole procedure is repeated 10 times, to obtain an ensemble of reconstructions. The mean and rms deviation refer to such an ensemble, as

$$\delta\Sigma = \left(\langle\Sigma^2\rangle - \langle\Sigma\rangle^2\right)^{\frac{1}{2}}. \quad (3)$$

Each map of Σ and $\delta\Sigma/\Sigma$ comes out of 90 separate reconstructions at different resolutions. The typical computational requirement is 50 hours × 16 cores.

A simulated lens at redshift 0.1 was next created with five Plummers positioned such that the configuration resembles the inner region of Abell 3827. Sources were put at different redshifts, as follows.

(i) Three-source case: three sources at $z = 0.2$ were were given as input.
(ii) Four-source case: a fourth source at $z = 0.4$ was added.
(iii) Five-source cases: a fifth source at $z = 1.0$ was added.

The resulting images, along with caustics and critical curves, is shown in Figure 3). Results from these are shown in Figure 4. The top row of the figure shows the mass maps Σ. The second row shows $\delta\Sigma/\Sigma$, or the fractional rms deviation. The third row shows $\Delta\Sigma/\delta\Sigma$ where $\Delta\Sigma$ is the (absolute) actual deviation of the reconstructed mass map from the real mass map. If $\delta\Sigma$ were close to $\Delta\Sigma$, we could simply take the rms deviation as the uncertainty. In fact the rms deviation under-estimates the true error by about a factor of two. That can be read off the bottom row of Figure 4, which plots the cumulative distribution of $\Delta\Sigma/\delta\Sigma$.

The main result from this test is that the rms deviation times two is a reasonable approximation of the errors. In addition, we can also read off some qualitative features from Figure 4. First, the spur or handle-like feature to the lower right is recovered in the lens reconstruction in all cases, even if not perfectly reproduced. Second, the maps get more accurate as more sources, especially at different redshifts, are introduced.

We conclude that GRALE is able to find offsets as well as extended structures (if any) in lenses.

3 RECONSTRUCTION OF THREE REAL CLUSTERS

In this Section we do mass reconstructions of three galaxy-clusters, and present these with their accompanying mass error maps. The two sets of maps for each cluster allow us to judge whether light-follows-mass (LFM) is a good assumption. We defer the discussion of the implications of the deviations from LFM to Section 4.

3.1 Abell 3827

Abell 3827 is a lensing cluster at redshift 0.099. Three multiply lensed image systems have been identified (Carrasco et al. 2010) belonging to three sources at redshift 0.204, most probably different parts of the same source. Another big arc is identified belonging to a source at redshift 0.408, but its multiply imaged counterpart has not yet been identified. A mass map based on these images (Williams & Saha 2011) indicates a dark extended clump, offset by $\sim 6\,\mathrm{kpc}$ from the brightest of the four or five ellipticals in the cluster core. This offset, if confirmed, would afford us a unique opportunity to examine and understand

the dynamics in dense regions of clusters. One of the primary goals of this paper is to assess the reality of this offset and estimate its statistical significance. GRALE is a very different lens mass reconstruction method from the one used in Williams & Saha (2011), so detecting the offset with GRALE will lend credence to its reality.

Using the identified images we reconstructed the mass distribution in two ways, and then combined the results. These are displayed in the three rows of Figure 5.

First, we used the three image systems belonging to the sources at redshift 0.2. The first panel of the top row of Figure 5 shows a spur in the mass map, which is offset from the nearby elliptical galaxy (the right most of the five grey dots). The spur's location is similar to the location of the local overdensity reported in Williams & Saha (2011), so the offset is similar in both reconstructions. From the map of fractional rms deviation $\delta\Sigma/\Sigma$ (right panel of the first row) the spur appears to be significant; the rms deviation in that region is about 0.1 kg m^{-2}, and so the fractional error is about 10%. Since the structure appears to be extended and not a single clump, it is not obvious how to quantify it. We can nonetheless test its significance. We chose a circle of radius $5''$ (green circle) around the nearby elliptical. (The choice of size is somewhat arbitrary; other choices would also serve our purpose.) We then calculate the centre of mass within this circle, for each mass map within the ensemble, and mark them with green '+' signs in the middle panel of top row, which is a zoom on to the relevant region. All ten centroids are consistently displaced from the nearby galaxy (grey circle), by about $1.2''$. The average of the ten centroids is marked with a blue star symbol. We may interpret these results as a hypothesis test. The null hypothesis is that the cluster has no mass/galaxy offset, and the mass is centred on the galaxy light. A mass reconstruction could nonetheless put the aperture centroid displaced from the galaxy, simply from the stochastic element in the genetic algorithm — note that the mass reconstructions are not given any information about the cluster galaxies. If there is no mass offset, the model offsets would be random, and the change of all 10 mass reconstructions having an offset in the same direction would be only 10%. But the aperture centroids are consistently offset in the same region. Hence there does appear to be an offset, significant at 90% confidence, between the mass spur and the galaxy.

Second, we used all four image systems: three belonging to the sources at redshift 0.2 and one with source redshift 0.4. As mentioned before, no image counterpart of the latter has been identified, but there is a possibility of such a counter-image near the centre of the cluster. Accordingly, we allowed GRALE to produce extra images in that region. The corresponding mass maps are shown in the second row of Figure 5. This time the extent of the image region is larger, and the fraction rms between reconstructions (right panel) is smaller in the general region of the image at $z_s = 0.4$. A clear mass subpeak is seen near the elliptical, offset from it by $\sim 4''$ or ~ 7 kpc. To be consistent with the previous case, we again calculate the centre of mass, or centroid, in a circular region of radius $5''$. Individual centroids are marked with green '$\times$' signs, and their average is the blue star. Again the offset is detected at a significance similar to the one above.

Finally, we then combined the two sets of ensembles described above, for a total of twenty individual maps. The bottom row of Figure 5 shows the average mass map, and the map of $\delta\Sigma/\Sigma$ for the combined ensemble. The conclusion remains unchanged.

3.2 Abell 2218

Abell 2218 is a well known and much studied lensing cluster (e.g., Abdelsalam et al. 1998). Like other rich clusters, it has been used in the recent years as a cosmic telescope (Altieri et al. 2010; Hopwood et al. 2010; Knudsen et al. 2010) to get a better view of distant or faint galaxies. The strong lensing region is somewhat larger on the sky than in Abell 3827, and the greater redshift, $z_l = 0.175$, implies a larger physical scale, 3 kpc arcsec^{-1}.

We reconstructed the cluster using the four most secure strong lensing systems. Figure 6 shows the mass map (left panel) and fraction rms dispersion between the ten individual maps of the ensemble (right panel). While apparent offsets are visible between galaxies (grey dots) and mass in the central region of the cluster, these are not significant, because rms in that region is comparable to the typical value of the surface mass density. Significant offsets are seen around the lower right mass clump, where the rms dispersion between mass maps is low. In the central panel we show a zoom of that region, similar to that in the middle panel of Figure 5. The green '+' signs represent the local mass peaks (not centroids as in the case of A3827) of individual reconstructions, which are displaced from the nearest cluster galaxies, represented by grey dots in the upper right of that panel.

3.3 Abell 1689

Abell 1689, at redshift 0.183, is perhaps the best known lensing cluster, containing over a hundred lensed images from at least thirty background sources extending to high redshifts (Broadhurst et al. 2005). Our reconstruction of its mass is shown in Figure 7. As with Abell 2218, the mass map and the rms maps are in the left and right panels. There are no significant mass/light offsets in this cluster. To illustrate that, in the central panel we show a zoom into the central region, where the mass peaks of the ten individual maps are shown as green '+' symbols. Their distribution with respect to the central cluster galaxy (grey dot) is consistent with the two being coincident.

Because the cluster has many multiply imaged systems spanning a wide range of redshifts it is possible to test if there are line of sight (los) structures that have affected the positions of images. We divided the multiply lensed sources into two groups, the low redshift system (LRS) and high redshift system (HRS). LRS consists of a total of three multiply imaged systems with five, three and three (total of eleven)

images at redshifts 2.54, 1.99 and 1.98, respectively. HRS consists of a total of two multiply imaged systems with two and five (total of seven) images at redshifts 4.53 and 2.99, respectively. We then carried out mass reconstruction for A1689 using LRS and HRS separately. The two mass maps are shown in Figure 8, in the upper left and upper middle panels, respectively. The corresponding fraction rms distributions are shown below each map. The upper right panel is the difference between HRS and LRS maps divided by the rms of the LRS maps ($\Delta\Sigma/\delta\Sigma$). Most of this map is consistent with a uniform surface mass density of low amplitude, about a factor of ten below the critical surface mass density. This could be due to steepness, or mass sheet degeneracy which affected one map more than the other. The only prominent feature is a mass excess in the HRS map, compared to the LRS map, centred at around $(-20'', 35'')$. The $\delta\Sigma$ maps for both HRS and LRS are both low in that region, suggesting that the structure is real. We interpret this feature as a los structure, probably in the redshift range 2–3. Another test of the structure's significance is shown in the lower right, which contains a histogram of the upper right plot $\Delta\Sigma/\delta\Sigma$ (pixelwise). The putative los structure contributes to the tail extending beyond the right edge of the distribution. The corresponding lensing mass would be $\sim 10^{13} M_\odot$ if the structure were at the same same redshift at A1689, but since the structure can only be at $z > 2.5$, the critical density and hence the lensing mass are much lower — a few times $10^{12} M_\odot$ — amounting to a modest galaxy group. There is another feature at $(-50'', -60'')$, but it is outside the image circle, and the $\delta\Sigma$ in that region says that it is not significant.

4 DISCUSSION

Gravitational lensing offers a unique opportunity to study the distribution of matter in clusters of galaxies. Free-form reconstruction methods take full advantage of this. Our synthetic tests show that GRALE recovers the mass distribution well, and the concomitant errors provide a reliable guide to assessing the significance of various mass features. The test case in Figure 2 and 4 shows no spurious offsets in the mass maps.

Reconstructions of the three real lensing clusters indicate some curious features. In two clusters we see offsets between the optical light and the nearest mass concentrations. The form of the offsets is not resolved: they could be distinct peaks in the projected mass distribution; or they could be spurs that extend from a peak that itself coincides with the galaxy light; or the offsets could very lopsided dark halos around galaxies. (We emphasize that not all offsets seen in the reconstructed mass maps are significant, but only those that pass the statistical significance tests.) A caveat to bear in mind is the assumption that the observed image positions are accurate. Because lensed images are often faint, have low surface brightness and are superimposed on brighter cluster galaxies, image identification is not always straightforward. It is thus conceivable that some images have been misidentified. But assuming the image identifications are all valid, confirmation by independent techniques is desirable. Lens reconstruction methods not assuming light traces mass in some way include Lensview (Wayth & Webster 2006), LensPerfect (Coe et al. 2008) and PBL (Deb et al. 2008) and any of these would be suitable. If the mass/galaxy offsets are confirmed, they would lead to interesting conclusions about the nature of clusters and dark-matter.

In general, several reasons for offsets are possible. Superimposed, but dynamically unrelated line of sight structures could contribute lensing mass, with no apparent associated light, especially if the structures are considerably further away from us than the main lensing cluster. However, we argue that the offset in A3827, is not due to the line of sight structure because of the very low redshifts of the sources. In A2218 line of sight structures are also unlikely to be the cause because only a very concentrated and massive los structure can contribute significantly in the vicinity of a massive clump within a cluster. Such chance superposition are expected to be rare.

Line of sight structures are more likely to make a contribution away from mass concentrations within the cluster, where cluster projected densities are lower. This can be illustrated with dark-matter N-body simulations. The blue lines in Figure 9 are the isodensity contours of the total projected mass in a cylinder centered on a halo whose virial radius is the radius of the window, while the red lines are the contours of the projected mass inside the virial sphere of the cluster. We caution that these plots were made with a limited line of sight depth of about comoving 90 Mpc (Simulations courtesy Jürg Diemand; Diemand et al. (2004)). The black contours mark regions where the fractional mass excess due to the line of sight structures (and not the mass within the virial sphere) amount to 25% of total. The top two panels show examples where the contribution from the los material is typical, while the bottom two panels present two cases with the most contribution (out of a total of 100 lines of sight). Even though the length of the cylinder is not large, the plots show that los structures cannot make a significant contribution where the cluster density is high. However, such structures can make a significant contribution at some distance away from the cluster centre.

In A1689 we might be seeing such a line of sight structure. After subtracting the mass reconstruction based on high-z sources (HRS) from that based on low-z sources (LRS) we see a mass concentration about 30 arcsec, or 100 kpc from cluster center. It is statistically significant (it contributes to the tail of the distribution shown in Fig. 8 which extend beyond the right edge of the plot) but is not associated with bright cluster galaxies. We interpret it as arising from a structures between the $z \approx 2$ and 3.

If not line of sight structure, what else can be responsible for mass-light offsets seen in A3827 and A2218? Offsets could be intrinsic to the cluster, and be due to manifestations of known physics, like gravity, and hydro-

dynamics of the gas, or new physics, such as self-scattering of dark matter. Offsets in merging clusters have been observed, but mostly between the dark matter and the X-ray emitting gas components (Clowe et al. 2006; Hsu et al. 2013; Clowe et al. 2012). In the outskirts of Abell 2744 a separation between dark matter and galaxy components is also seen (Merten et al. 2011), and in the merging cluster CL0152-1357 an offset between Sunyaev-Zel'dovich effect and X-ray peaks has been detected (Molnar et al. 2012). Most of these offsets are on larger scales then what we detect in this work. For smaller scale offsets early stage mergers are probably not the cause, and different set of causes has to be considered.

One of the possibly relevant gravitational effects is the oscillation or wobbling of a galaxy, such as a BCG around the bottom of the gravitational potential. This has been observed in a sample of galaxy clusters as a displacement of the BCG from the lensing centroid (Zitrin et al. 2012). The distribution is displacements is wide, and peaks at roughly 10 kpc. Whether this is a likely explanation for the offsets in A3827 and A2218 is yet to be determined—the observed offsets are not for central cluster galaxies.

It is less likely, but still possible that the offsets are a consequence of tidal effects. These would strip the material from the galaxy symmetrically in the leading and trailing directions. Since the offsets in A3827 and A2218 do not show such symmetry, tidal effects are probably not the main cause.

Dynamical friction would create an asymmetric structure and would preferentially distort the distribution of dark matter and not stars if the former has a more extended distribution. A numerical simulation would be required to test this possibility.

The formation of a galaxy cluster is a complex process involving hydrodynamics of gas. It is possible that star formation induced by galaxy mergers within clusters would result in stars and dark matter halos offsets.

Finally, if dark-matter has non-negligible self-interaction cross-section, dark-matter particles of the galaxy halo would experience a drag force as the galaxy moves within the halo of the cluster. The nature of the resulting dark-matter features induced by these interactions may be consistent with those observed in A3827 and A2218, but detailed simulations are required (Kahlhoefer et al. 2014).

5 ACKNOWLEDGEMENT

LLRW would like to acknowledge the hospitality of ITP, Zurich.

REFERENCES

Abdelsalam H. M., Saha P., Williams L. L. R., 1998, AJ, 116, 1541
Altieri B. et al., 2010, A&A, 518, L17
Broadhurst T. et al., 2005, ApJ, 621, 53
Carrasco E. R. et al., 2010, ApJL, 715, L160
Charbonneau P., 1995, APJS, 101, 309
Clowe D., Bradač M., Gonzalez A. H., Markevitch M., Randall S. W., Jones C., Zaritsky D., 2006, ApJL, 648, L109
Clowe D., Markevitch M., Bradač M., Gonzalez A. H., Chung S. M., Massey R., Zaritsky D., 2012, ApJ, 758, 128
Coe D., Fuselier E., Benítez N., Broadhurst T., Frye B., Ford H., 2008, ApJ, 681, 814
Deb S., Goldberg D. M., Ramdass V. J., 2008, ApJ, 687, 39
Diemand J., Moore B., Stadel J., 2004, MNRAS, 352, 535
Duc P.-A., Poggianti B. M., Fadda D., Elbaz D., Cesarsky C., 2002, A&A, 382, 60
Harvey D., Massey R., Kitching T., Taylor A., Jullo E., Kneib J.-P., Tittley E., Marshall P. J., 2013a, MNRAS, 433, 1517
Harvey D. et al., 2013b, ArXiv:1310.1731
Hopwood R. et al., 2010, ApJL, 716, L45
Hsu L.-Y., Ebeling H., Richard J., 2013, MNRAS, 429, 833
Kahlhoefer F., Schmidt-Hoberg K., Frandsen M. T., Sarkar S., 2014, MNRAS, 437, 2865
Knudsen K. K., Kneib J.-P., Richard J., Petitpas G., Egami E., 2010, ApJ, 709, 210
Liesenborgs J., De Rijcke S., Dejonghe H., 2006, MNRAS, 367, 1209
Liesenborgs J., De Rijcke S., Dejonghe H., Bekaert P., 2007, MNRAS, 380, 1729
Liesenborgs J., De Rijcke S., Dejonghe H., Bekaert P., 2008, MNRAS, 389, 415
Liesenborgs J., De Rijcke S., Dejonghe H., Bekaert P., 2009, MNRAS, 397, 341
Merten J. et al., 2011, MNRAS, 417, 333
Molnar S. M., Hearn N. C., Stadel J. G., 2012, ApJ, 748, 45
Pello R., Le Borgne J. F., Sanahuja B., Mathez G., Fort B., 1992, A&A, 266, 6
Planck collaboration et al., 2013, ArXiv:1303.5075
Randall S. W., Markevitch M., Clowe D., Gonzalez A. H., Bradač M., 2008, ApJ, 679, 1173
Saha P., Read J. I., Williams L. L. R., 2006, ApJL, 652, L5
Sánchez A. G. et al., 2013, MNRAS, 433, 1202
Saro A., Mohr J. J., Bazin G., Dolag K., 2013, ApJ, 772, 47
Vikhlinin A. et al., 2009, ApJ, 692, 1033
Wayth R. B., Webster R. L., 2006, MNRAS, 372, 1187
Williams L. L. R., Saha P., 2011, MNRAS, 415, 448
Zitrin A., Bartelmann M., Umetsu K., Oguri M., Broadhurst T., 2012, MNRAS, 426, 2944
Zitrin A., Broadhurst T., Coe D., Liesenborgs J., Benítez N., Rephaeli Y., Ford H., Umetsu K., 2011, MNRAS, 413, 1753
Zitrin A. et al., 2010, MNRAS, 408, 1916

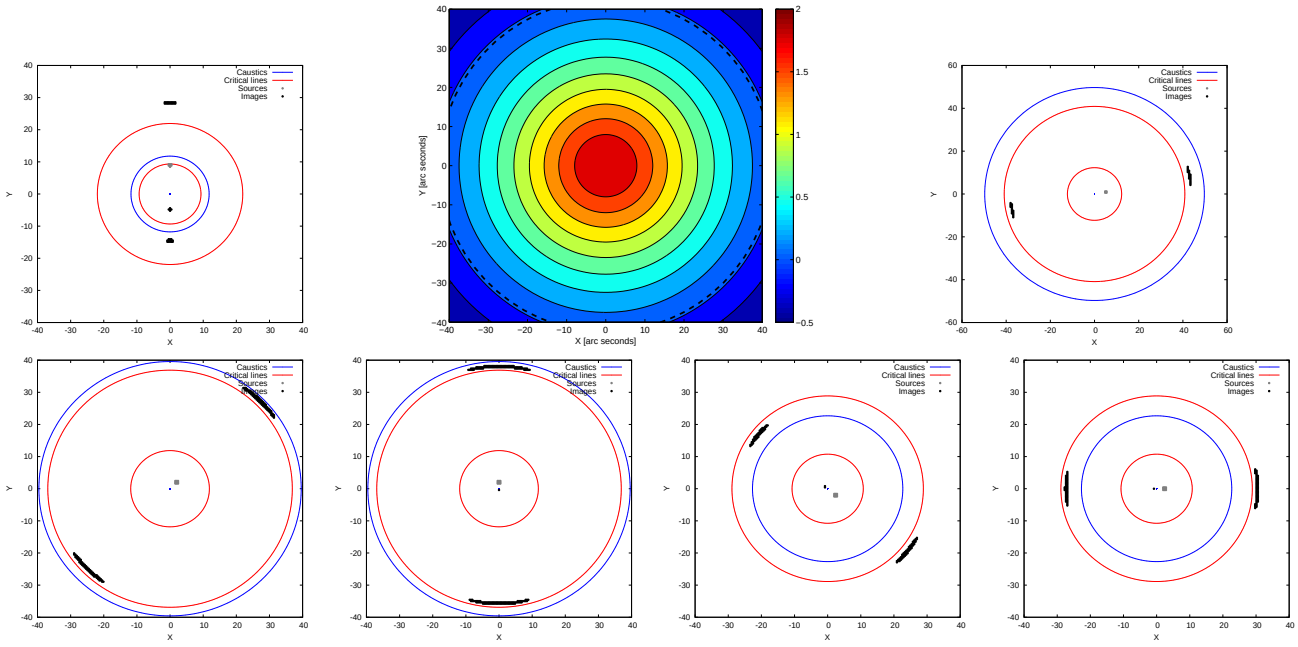

Figure 1. A circularly symmetric synthetic lens (centre top panel) and six image systems from sources at different redshifts. Sources are in grey, caustics are in blue, critical curves are in red. The contour lines in the synthetic lens are those of constant surface mass density; the color scale is in units of log (kg m^{-2}). The same scale is used in all figures in this paper. For reference, $\Sigma_{\rm crit}$ for $z_l = 0.1$ and $z_s = 0.2$ in a standard ΛCDM cosmology is 18.7 kg m^{-2}.

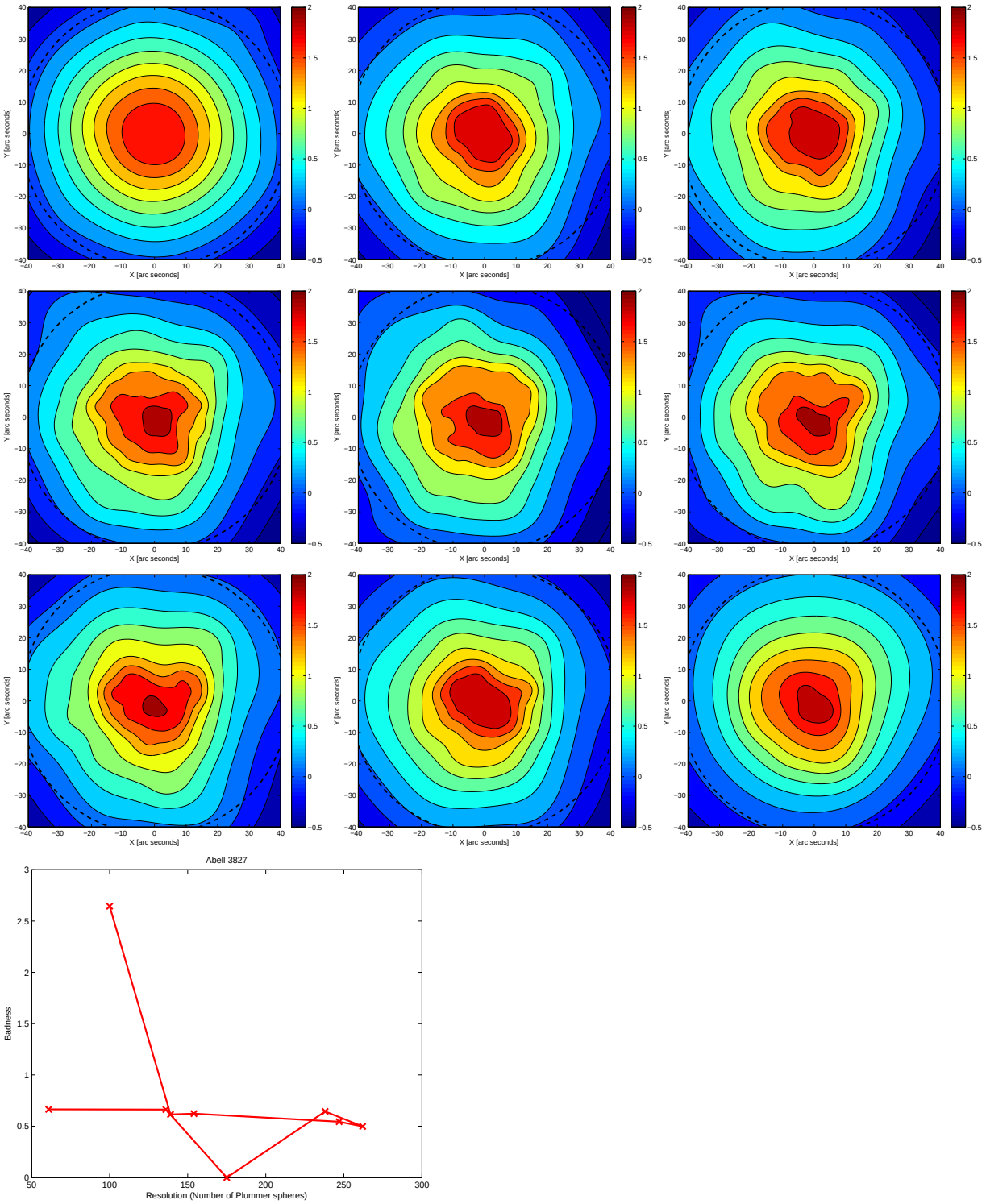

Figure 2. Reconstruction of the lens in Figure 1 from the data in that figure. The badness curve (bottom panel) shows that the best model is the third one (top right map in the grid of nine.) The dashed circle in each map delineates the modeled region. . The sequence of mass maps is in reading order (from top-left to bottom-right).

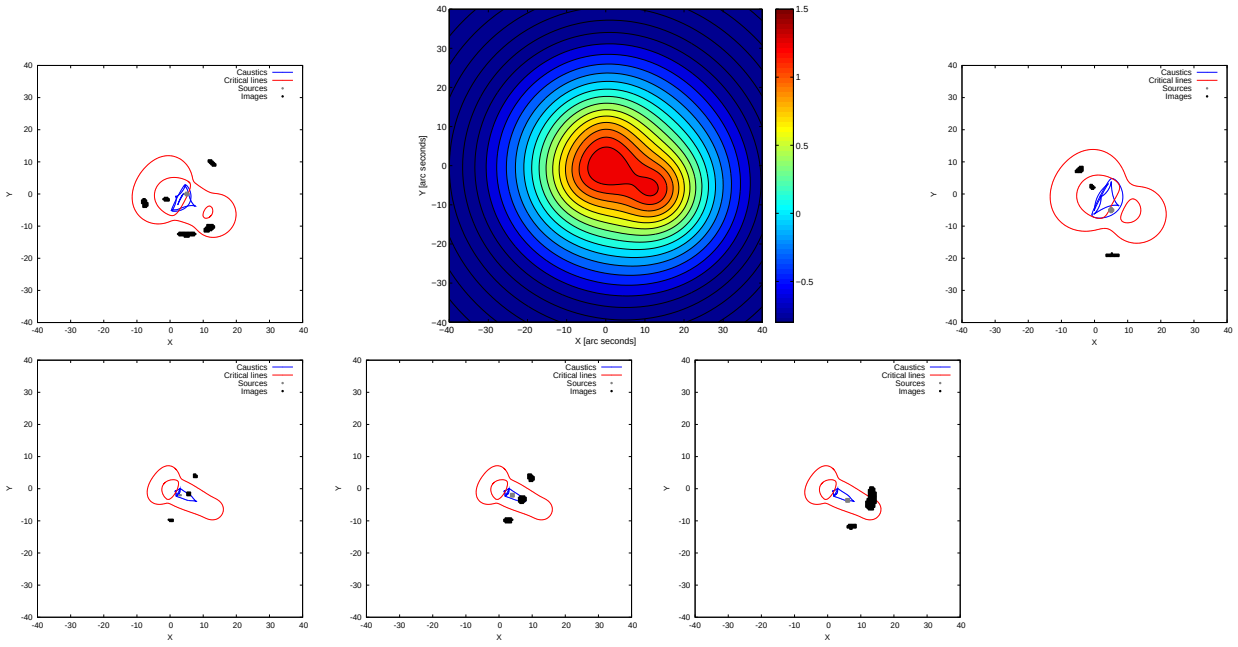

Figure 3. A synthetic lens with a main mass concentration and a nearby secondary mass peak. Five projected Plummer spheres are used to construct this lens. Image systems from five sources at different redshifts are shown in separate panels.

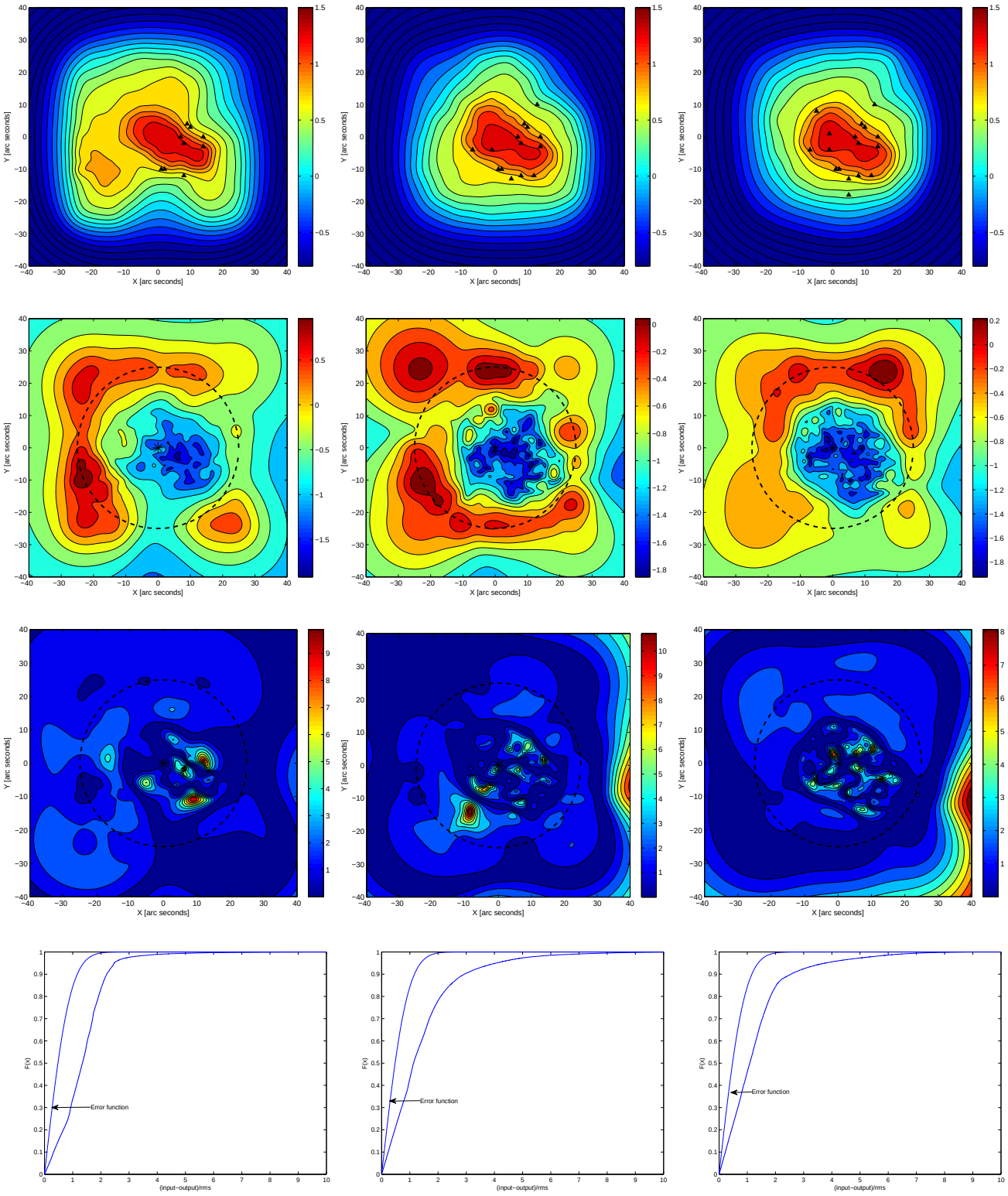

Figure 4. Reconstruction of the lens in Figure 3. Column 1: using three sources only, with the corresponding images shown as black triangles; column 2: using four sources; column 3: using all five sources. The top row shows average surface mass density Σ; units are same as in Figure 1. The second row shows the fractional rms deviation of ten reconstructions, $\delta\Sigma/\Sigma$. The third row contains $\Delta\Sigma/\delta\Sigma$ where $\Delta\Sigma$ is the pixelwise difference between the true map and the average reconstructed map. The bottom row shows the cumulative $\Delta\Sigma/\delta\Sigma$, along with the corresponding curve (marked 'error function') for Gaussian errors with dispersion $\delta\Sigma$. We conclude that the error estimate $\delta\Sigma$ needs to be multiplied by ~ 2 (or increased by 0.30 on a $\log_{10}$ scale). The worst cases are some very small regions (red in the lower panels) where $\log_{10}\Delta\Sigma$ should be increased by $\sim +1$.

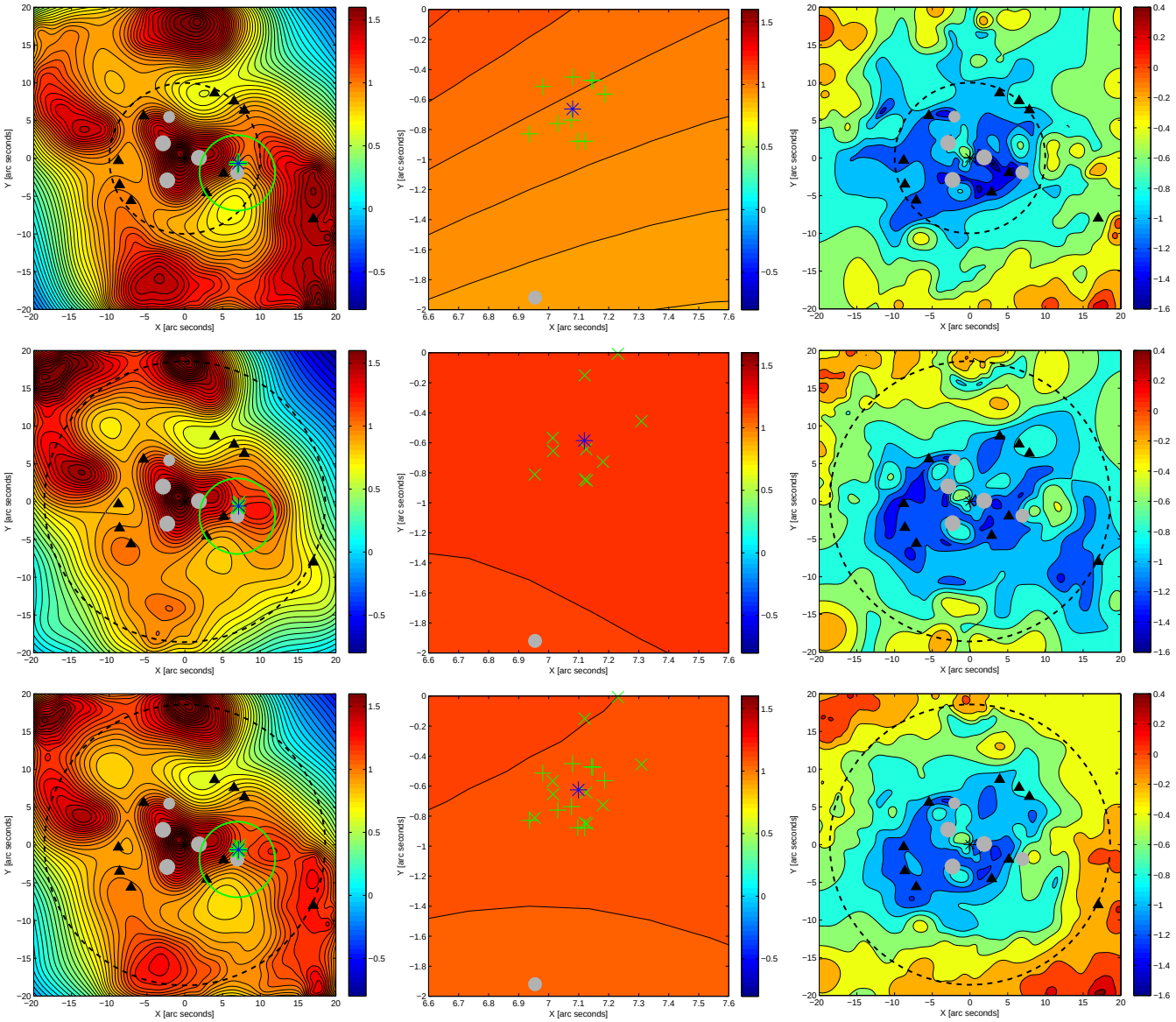

Figure 5. Mass reconstructions of A3827. North is up and East to the right. The scale is 1.82 kpc/arcsec. The upper row maps are an ensemble of ten maps, each obtained using only the nine images of the source at $z_s = 0.2$. The middle row shows an ensemble of ten maps, using nine images of the $z_s = 0.2$ source and the single image at $z_s = 0.4$. The bottom row combines both ensembles. The left column presents the average of the ten mass maps. The middle column is a zoom centered on the most luminous elliptical N1. The ten green '+' signs (top row) and '×' signs (middle row) represent centroids from ten individual maps of the mass within the green circle shown in the left column. The grey dot towards the bottom of the plots (in the middle column) is N1. The blue asterisk is the centroid of the average of the ten realisations. The right column shows the fractional rms deviation between the ten maps, $\delta\Sigma/\Sigma$.

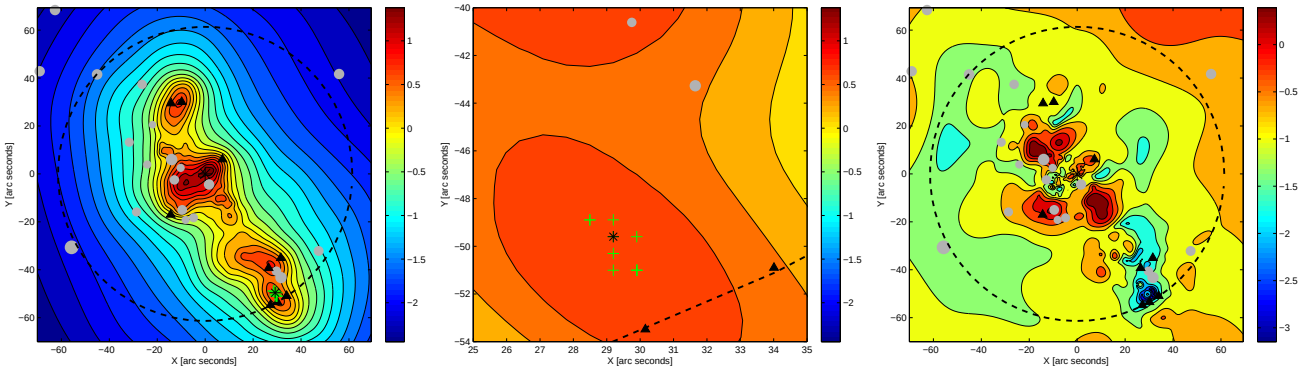

Figure 6. Mass map of A2218. North is up and East to the right. The average mass map (left column) and fractional rms (right column) are based on ten realisations. The central column shows the zoom of the region with mass-light offsets, and the green '+' signs are the local mass peaks from individual reconstructions. The scale is 3 kpc/arcsec. Galaxies with $R < 20$ (Pello et al. 1992) are marked with grey dots.

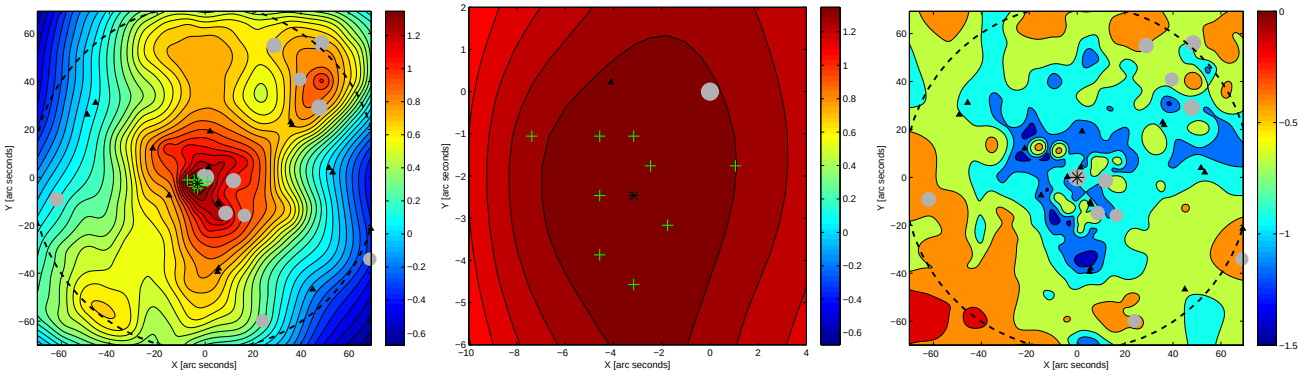

Figure 7. Mass maps of A1689. North is up and East to the right. The columns are similar to those in Fig. 6. Galaxy positions (Duc et al. 2002) also marked.

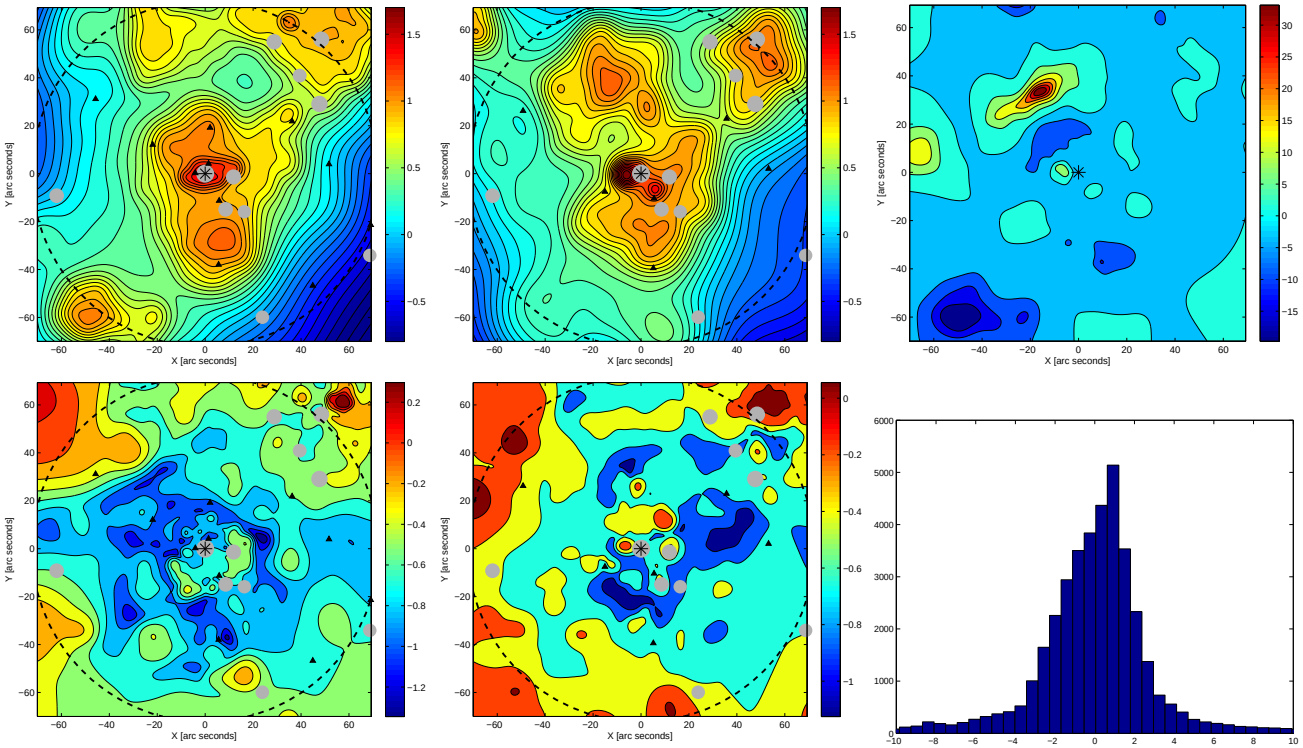

Figure 8. Test for the line of sight structure in A1689. Upper left and upper middle panels are the mass maps obtained using two separate sets of sources: at low and high redshifts respectively. Lower left and lower middle panels are the corresponding fractional rms maps. Upper right is the difference between the high-z (HRS) and the low-z (LRS) maps divided by the rms of the low-z maps (i.e., $\Delta\Sigma/\delta\Sigma$, which is dimensionless); the scale is linear. Note the apparent structure at higher z, near $(-20'', 35'')$. Lower right is the histogram of the map above it (pixelwise) $\Delta\Sigma/\delta\Sigma$.

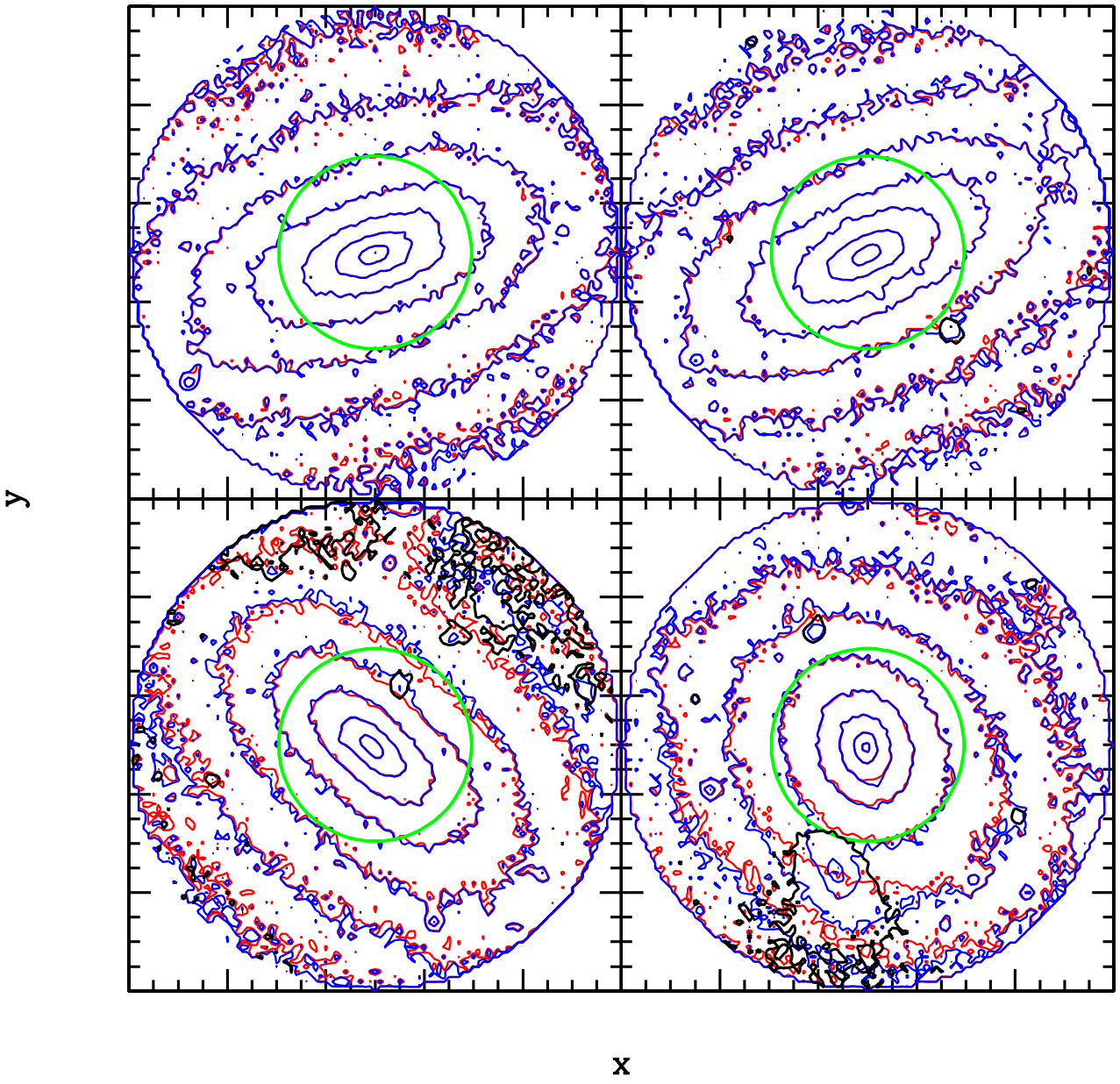

Figure 9. Density contours of projected mass centered on halos taken from dark matter only simulations (Diemand et al. 2004). The radius of the window is the virial radius, and the green circle marks the typical radius where lensed images will be formed. The red density contours are due to the halo mass interior to the virial sphere, while the blue contours are due to all projected mass within a cylinder of roughly 90 Mpc. The black contours mark regions where the fractional mass excess due to the line of sight structures (and not the mass within the virial sphere) amount to 25% of total. The top two panels show average lines of sight, while the bottom panels the two (out of 100) where los material makes the most contribution.